Deep-Sea Research II ∎ (∎∎∎∎) ∎∎∎–∎∎∎

Contents lists available at SciVerse ScienceDirect

Deep-Sea Research II

journal homepage: www.elsevier.com/locate/dsr2

Symmetric instability in the Gulf Stream

Leif N. Thomas [a,*], John R. Taylor [b], Raffaele Ferrari [c], Terrence M. Joyce [d]

[a] Department of Environmental Earth System Science, Stanford University, United States
[b] Department of Applied Mathematics and Theoretical Physics, University of Cambridge, United Kingdom
[c] Earth, Atmospheric and Planetary Sciences, Massachusetts Institute of Technology, United States
[d] Department of Physical Oceanography, Woods Hole Institution of Oceanography, United States

ARTICLE INFO

Keywords:
Fronts
Subtropical mode water
Upper-ocean turbulence
Ocean circulation energy

ABSTRACT

Analyses of wintertime surveys of the Gulf Stream (GS) conducted as part of the CLIvar MOde water Dynamic Experiment (CLIMODE) reveal that water with negative potential vorticity (PV) is commonly found within the surface boundary layer (SBL) of the current. The lowest values of PV are found within the North Wall of the GS on the isopycnal layer occupied by Eighteen Degree Water, suggesting that processes within the GS may contribute to the formation of this low-PV water mass. In spite of large heat loss, the generation of negative PV was primarily attributable to cross-front advection of dense water over light by Ekman flow driven by winds with a down-front component. Beneath a critical depth, the SBL was stably stratified yet the PV remained negative due to the strong baroclinicity of the current, suggesting that the flow was symmetrically unstable. A large eddy simulation configured with forcing and flow parameters based on the observations confirms that the observed structure of the SBL is consistent with the dynamics of symmetric instability (SI) forced by wind and surface cooling. The simulation shows that both strong turbulence and vertical gradients in density, momentum, and tracers coexist in the SBL of symmetrically unstable fronts.

SI is a shear instability that draws its energy from geostrophic flows. A parameterization for the rate of kinetic energy (KE) extraction by SI applied to the observations suggests that SI could result in a net dissipation of 33 mW m^{-2} and 1 mW m^{-2} for surveys with strong and weak fronts, respectively. The surveys also showed signs of baroclinic instability (BCI) in the SBL, namely thermally direct vertical circulations that advect biomass and PV. The vertical circulation was inferred using the omega equation and used to estimate the rate of release of available potential energy (APE) by BCI. The rate of APE release was found to be comparable in magnitude to the net dissipation associated with SI. This result points to an energy pathway where the GS's reservoir of APE is drained by BCI, converted to KE, and then dissipated by SI and its secondary instabilities. Similar dynamics are likely to be found at other strong fronts forced by winds and/or cooling and could play an important role in the energy balance of the ocean circulation.

1. Introduction

It has long been recognized that baroclinic instability plays an important role in the energetics of the Gulf Stream (GS) (e.g. Gill et al., 1974). The instability extracts available potential energy (APE) from the current converting it into kinetic energy (KE) on the mesoscale. Turbulence on the mesoscale is highly constrained by the Earth's rotation and thus follows an inverse cascade, with KE being transferred away from the small scales where viscous dissipation can act (Ferrari and Wunsch, 2009). Thus the pathway along which the energy of the GS is ultimately lost cannot be direct through the action of the mesoscale alone. Submesoscale instabilities have been implicated as mediators in the dissipation of the KE of the circulation as they can drive a forward cascade (Capet et al., 2008; Molemaker et al., 2010). One submesoscale instability that could be at play in the GS and that has been shown to be effective at removing KE from geostrophic currents is symmetric instability (SI) (Taylor and Ferrari, 2010; Thomas and Taylor, 2010).

In the wintertime, the strong fronts associated with the GS experience atmospheric forcing that makes them susceptible to SI. A geostrophic current is symmetrically unstable when its Ertel potential vorticity (PV) takes the opposite sign of the Coriolis parameter as a consequence of its vertical shear and horizontal density gradient (Hoskins, 1974). The strongly baroclinic GS is thus preconditioned for SI. SI is a shear instability that extracts KE from geostrophic flows (Bennetts and Hoskins, 1979). Under destabilizing atmospheric forcing (i.e. forcing that tends to reduce

* Corresponding author.
E-mail address: leift@stanford.edu (L.N. Thomas).

0967-0645/$ - see front matter © 2013 Elsevier Ltd. All rights reserved.
http://dx.doi.org/10.1016/j.dsr2.2013.02.025

the PV) the rate of KE extraction by SI depends on the wind-stress, cooling, and horizontal density gradient (Taylor and Ferrari, 2010; Thomas and Taylor, 2010).

Preliminary analyses of observations from the eastern extension of the GS taken during the winter as part of the CLIvar MOde water Dynamic Experiment (CLIMODE, e.g. Marshall et al., 2009) suggest that SI was present (Joyce et al., 2009). In this paper CLIMODE observations that sampled the GS in both the east and west will be analyzed to characterize the properties of SI in the current and its effects on the surface boundary layer. Particular emphasis will be placed on assessing the relative contributions of SI and baroclinic instability to the energy balance of the GS under strong wintertime forcing. Both the energetics and boundary layer dynamics that will be discussed are shaped by small-scale turbulent processes. While microstructure measurements were made as part of CLIMODE (e.g. Inoue et al., 2010), these processes were not explicitly measured during the surveys described here, therefore to study their properties a large eddy simulation (LES) configured with flow and forcing parameters based on the observations has been performed. Before presenting the analyses of the observations and LES an overview of the dynamics of wind and cooling forced SI will be given.

2. Dynamics of forced symmetric instability

2.1. Potential vorticity and overturning instabilities

A variety of instabilities can develop when the Ertel potential vorticity (PV), q, takes the opposite sign of the Coriolis parameter (Hoskins, 1974), i.e.

$$fq = f(f\hat{k} + \nabla \times \mathbf{u}) \cdot \nabla b < 0, \tag{1}$$

where f is the Coriolis parameter, $\mathbf{u}$ is the velocity, and $b = -g\rho/\rho_o$ is the buoyancy (g is the acceleration due to gravity and ρ is the density). The instabilities that arise take different names depending on whether the vertical vorticity, stratification, or baroclinicity of the fluid is responsible for the low PV. For barotropic flows where $f\zeta_{abs}N^2 < 0$ ($\zeta_{abs} = f - u_y + v_x$) and $N^2 > 0$ the instabilities that arise are termed *inertial* or *centrifugal*. *Gravitational instability* occurs when $N^2 < 0$. In strongly baroclinic flows, the PV can take the opposite sign of f even if $f\zeta_{abs}N^2 > 0$. This is illustrated by decomposing the PV into two terms

$$q = q_{vert} + q_{bc}, \tag{2}$$

one associated with the vertical component of the absolute vorticity and the stratification

$$q_{vert} = \zeta_{abs}N^2, \tag{3}$$

the other attributable to the horizonal components of vorticity and buoyancy gradient

$$q_{bc} = \left(\frac{\partial u}{\partial z} - \frac{\partial w}{\partial x}\right)\frac{\partial b}{\partial y} + \left(\frac{\partial w}{\partial y} - \frac{\partial v}{\partial z}\right)\frac{\partial b}{\partial x}. \tag{4}$$

Throughout the rest of the paper we assume that the flows we are considering are to leading order in geostrophic balance. For a geostrophic flow, $\mathbf{u}_g$, it can be shown using the thermal wind relation that (4) reduces to

$$q^g_{bc} = -f\left|\frac{\partial \mathbf{u}_g}{\partial z}\right|^2 = -\frac{1}{f}|\nabla_h b|^2, \tag{5}$$

so that fq^g_{bc} is a negative definite quantity, indicating that the baroclinicity of the fluid always reduces the PV. When $|fq^g_{bc}| > fq_{vert}$, with $fq_{vert} > 0$, the instability that develops is termed *symmetric instability* (SI).

The instability criterion can equivalently be expressed in terms of the balanced Richardson number. Namely, the PV of a geostrophic flow is negative when its Richardson number

$$Ri_B = \frac{N^2}{(\partial \mathbf{u}_g/\partial z)^2} \equiv \frac{f^2N^2}{|\nabla_h b|^2} \tag{6}$$

meets the following criterion:

$$Ri_B < \frac{f}{\zeta_g} \quad \text{if } f\zeta_g > 0, \tag{7}$$

where $\zeta_g = f + \nabla \times \mathbf{u}_g \cdot \hat{k}$ is the vertical component of the absolute vorticity of the geostrophic flow (Haine and Marshall, 1998). In condition (7) we have excluded barotropic, centrifugal/inertial instability which arises when $f\zeta_g < 0$. If we introduce the following angle:

$$\phi_{Ri_B} = \tan^{-1}\left(-\frac{|\nabla_h b|^2}{f^2N^2}\right), \tag{8}$$

instability occurs when

$$\phi_{Ri_B} < \phi_c \equiv \tan^{-1}\left(-\frac{\zeta_g}{f}\right). \tag{9}$$

This angle is not only useful for determining when instabilities occur but it can also be used to distinguish between the various instabilities that can result. These instabilities can be differentiated by their sources of KE which vary with ϕ_{Ri_B}.

2.2. Energetics

The overturning instabilities that arise when $fq < 0$ derive their KE from a combination of shear production and the release of convective available potential energy (Haine and Marshall, 1998). The relative contributions of these energy sources to the KE budget differ for each instability. For a basic state with no flow and an unstable density gradient, pure gravitational instability is generated that gains KE through the buoyancy flux

$$\text{BFLUX} = \overline{w'b'} \tag{10}$$

(the overline denotes a spatial average and primes the deviation from that average). With stable stratification, no vertical shear, and $f\zeta_g < 0$, centrifugal/inertial instability forms and extracts KE from the laterally sheared geostrophic current at a rate given by

$$\text{LSP} = -\overline{\mathbf{u}'v_{s'}} \cdot \frac{\partial \overline{\mathbf{u}}_g}{\partial s}, \tag{11}$$

where s is the horizontal coordinate perpendicular to the geostrophic flow and v_s is the component of the velocity in that direction. For a geostrophic flow with only vertical shear, $N^2 > 0$, and $fq < 0$ SI develops and extracts KE from the geostrophic flow at a rate given by the geostrophic shear production

$$\text{GSP} = -\overline{\mathbf{u}'w'} \cdot \frac{\partial \overline{\mathbf{u}}_g}{\partial z}. \tag{12}$$

For an arbitrary flow with $fq < 0$, depending on the strength and sign of the stratification and vertical vorticity, and the magnitude of the thermal wind shear the instabilities that result can gain KE through a combination of the buoyancy flux and shear production terms (11) and (12). A linear instability analysis applied to a simple basic state with $fq < 0$ described in the appendix illustrates that the partitioning between energy sources is a strong function of ϕ_{Ri_B} and ϕ_c. As schematized in Fig. 1 and described below these two angles can thus be used to distinguish between the various modes of instability.

For unstable stratification ($N^2 < 0$) and $-180^\circ < \phi_{Ri_B} < -135^\circ$, gravitational instability develops, with BFLUX/GSP $\gg 1$, while for $-135^\circ < \phi_{Ri_B} < -90^\circ$, a hybrid gravitational/symmetric instability

Please cite this article as: Thomas, L.N., et al., Symmetric instability in the Gulf Stream. Deep-Sea Res. II (2013), http://dx.doi.org/10.1016/j.dsr2.2013.02.025

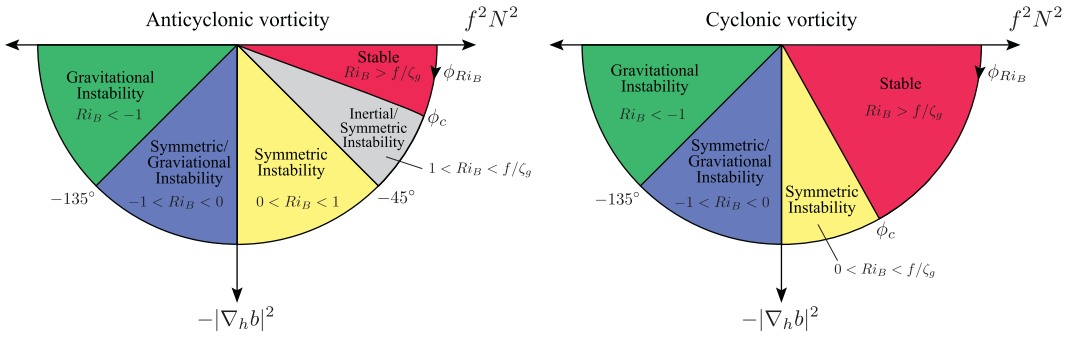

Fig. 1. Schematic illustrating the relation between the angle ϕ_{Ri_B} (8) to the various overturning instabilities that arise when $fq<0$ and the vorticity is anticyclonic (left) and cyclonic (right). The dependence of ϕ_{Ri_B} on the baroclinicity and stratification is also indicated.

develops, where both the buoyancy flux and GSP contribute to its energetics.

For stable stratification and cyclonic vorticity (i.e. $\zeta_g/f>1$) the instability that forms when

$$-90^\circ<\phi_{Ri_B}<\phi_c \quad \text{with } \phi_c<-45^\circ \tag{13}$$

derives its energy primarily via GSP and thus can be characterized as SI. For $N^2>0$ and anticyclonic vorticity (i.e. $\zeta_g/f<1$) both the LSP and GSP contribute to the energetics of the instabilities in varying degrees depending on ϕ_{Ri_B}. Specifically, GSP/LSP >1 and SI is the dominant mode of instability when

$$-90^\circ<\phi_{Ri_B}<-45^\circ \quad \text{with } \phi_c>-45^\circ. \tag{14}$$

When $-45^\circ<\phi_{Ri_B}<\phi_c$, a hybrid symmetric/centrifugal/inertial instability develops, where both the GSP and LSP contribute to its energetics.

In this sense, ϕ_{Ri_B} is analogous to the Turner angle which is used to differentiate between the gravitational instabilities: convection, diffusive convection, and salt fingering that can arise in a water column whose density is affected by both salinity and temperature (Ruddick, 1983). The parameter ϕ_{Ri_B} is also useful because it effectively remaps an infinite range of balanced Richardson numbers, $-\infty<Ri_B<\infty$, onto the finite interval $-180^\circ<\phi_{Ri_B}<0^\circ$.

2.3. Finite amplitude symmetric instability

As with many instabilities that have reached finite amplitude, turbulence generated by SI eventually adjusts the background flow so as to push the system to a state of marginal stability (Thorpe and Rotunno, 1989). For SI this corresponds to a geostrophic flow with $q=0$, a balanced Richardson number

$$Ri_{q=0}=\frac{f}{\zeta_g}, \tag{15}$$

and non-zero stratification

$$N^2_{q=0}=\frac{|\nabla_h b|^2}{f\zeta_g}. \tag{16}$$

This is in contrast to finite-amplitude pure gravitational instability which sets the PV to zero by homogenizing density (Marshall and Schott, 1999). SI and its secondary instabilities drive the PV towards zero by mixing waters with oppositely signed PV together. SI in the SBL thus leads to a restratification of the mixed layer. It should be noted that the upper ocean can be restratified by baroclinic instability as well, but via a different mechanism: the release of available potential energy by eddy-driven overturning which can occur even if $fq>0$ (Fox-Kemper et al., 2008).

In pushing the system to a state with $q=0$, SI damps itself out (Taylor and Ferrari, 2009). SI can be sustained however if it is forced by winds or buoyancy fluxes that generate frictional or diabatic PV fluxes at the surface of the ocean that tend to drive $fq<0$ and thus compensate for PV mixing by SI (Thomas, 2005; Taylor and Ferrari, 2010). Changes in PV are caused by convergences/divergences of a PV flux

$$\frac{\partial q}{\partial t}=-\nabla\cdot\mathbf{J}, \tag{17}$$

$\mathbf{J}=\mathbf{u}q+\nabla b\times\boldsymbol{F}-(f\hat{k}+\nabla\times\mathbf{u})\mathcal{D}$, which has an advective component and two non-advective constituents arising from frictional or non-conservative forces, $\boldsymbol{F}$, and diabatic processes, $\mathcal{D}\equiv Db/Dt$ (Marshall and Nurser, 1992). Therefore, in the upper ocean, the necessary condition for fq to be reduced and forced SI (FSI) to be sustained is

$$f(J^z_F+J^z_{\mathcal{D}})|_{z=0}>0, \tag{18}$$

where the vertical components of the frictional and diabatic PV fluxes are

$$J^z_F=\nabla_h b\times\boldsymbol{F} \tag{19}$$

and

$$J^z_{\mathcal{D}}=-\zeta_{abs}\mathcal{D}. \tag{20}$$

When (18) is met, PV is extracted from (injected into) the ocean in the Northern (Southern) Hemisphere thus pushing the PV in the surface boundary layer (SBL) towards the opposite sign of f. As shown in Thomas (2005), (18) can be related to the atmospheric forcing and horizontal density gradient. Specifically, FSI can occur if

$$\text{EBF}+B_o>0, \tag{21}$$

where B_o is the surface buoyancy flux and $\text{EBF}=\mathbf{M}_e\cdot\nabla_h b|_{z=0}$ is the *Ekman buoyancy flux* ($\mathbf{M}_e=\boldsymbol{\tau}_w\times\hat{\boldsymbol{z}}/\rho_o f$ is the Ekman transport), the measure of the rate at which Ekman advection of buoyancy can re- or destratify the SBL (Thomas and Taylor, 2010). From thermal wind balance, $\text{EBF}=\rho_o^{-1}|\boldsymbol{\tau}_w||\partial\boldsymbol{u}_g/\partial z|_{z=0}|\cos\theta$, where θ is the angle between the wind vector and geostrophic shear. Therefore, in the absence of buoyancy fluxes, condition (21) is satisfied when the winds have a *down-front* component, i.e. $-90^\circ<\theta<90^\circ$.

2.4. Criteria for forced symmetric instability

The sign of the combined Ekman and surface buoyancy fluxes in Eq. (21) is a necessary but not sufficient criteria for FSI. When Eq. (21) is met, the surface buoyancy is reduced, thereby destabilizing the water column. The stratification in the boundary layer is set by a competition between restratification by frontal circulations and mixing of the density profile by convection resulting from the surface forcing. The competition between restratification by FSI and surface forcing was studied in detail by Taylor and Ferrari (2010). They found that turbulence and stratification in

Please cite this article as: Thomas, L.N., et al., Symmetric instability in the Gulf Stream. Deep-Sea Res. II (2013), http://dx.doi.org/10.1016/j.dsr2.2013.02.025

the SBL could be described in terms of two distinct layers. Near the surface in a 'convective layer', $z > -h$, the buoyancy flux is positive, convective plumes develop, and the density profile remains relatively unstratified. The convective layer can be shallower than the depth of the SBL, H, which is defined as the depth where the bulk, balanced Richardson number equals one

$$Ri_{bulk}|_{z=-H} = \frac{H\Delta b}{(\Delta u_g)^2} \equiv 1, \tag{22}$$

where Δ refers to the change in the quantity from the surface to $z=-H$. Below the convective layer, for $-H < z < -h$, restratification by FSI wins the competition with the convective forcing, and the boundary layer restratifies.

The relative sizes of the convective layer depth, h, and the SBL depth, H, provide a measure of the importance of restratification by FSI. When $h/H \simeq 1$, convection dominates and the SBL remains unstratified. On the other hand, when

$$\frac{h}{H} \ll 1, \tag{23}$$

FSI dominates over convection and wind-driven turbulence and is able to restratify a large fraction of the SBL. Taylor and Ferrari (2010) derived a scaling for the convective layer depth, h, in terms of the surface forcing, SBL depth, and frontal strength

$$\frac{|\nabla_h b|^2}{f^2}(B_o + \mathrm{EBF})^{1/3} h^{4/3} = c\left[(B_o + \mathrm{EBF})\left(1 - (1+\alpha+\beta)\frac{h}{H}\right)\right], \tag{24}$$

where $c \simeq 14$ is an empirical scaling constant, and α and β are entrainment coefficients. Since the entrainment coefficients result in a relatively small modification to the SBL depth, we will neglect them here. We have also neglected the effects of surface gravity waves and Langmuir cells, which could play an important role in the turbulence of the SBL for conditions where the friction velocity $u_* = \sqrt{|\tau_w|/\rho_o}$ is weaker than the Stokes drift (McWilliams et al., 1997).

In order to illustrate the role of frontal baroclinicity, it is useful to rewrite (24) in terms of the velocity scales associated with the surface forcing and thermal wind

$$\left(\frac{h}{H}\right)^4 - c^3\left(1-\frac{h}{H}\right)^3\left(\frac{w_*^3}{|\Delta u_g|^3} + \frac{u_*^2}{|\Delta u_g|^2}\cos\theta\right)^2 = 0, \tag{25}$$

where $w_* = (B_o H)^{1/3}$ is the convective velocity and $\Delta u_g = |\partial \mathbf{u}_g/\partial z| H$ is the change in geostrophic velocity across the SBL, and θ is the wind angle defined above. For strongly baroclinic flows, where $\Delta u_g \gg u_*$ and $\Delta u_g \gg w_*$

$$\frac{h}{H} \to c^{3/4}\left[\frac{w_*^3}{|\Delta u_g|^3} + \left(\frac{u_*^2}{|\Delta u_g|^2}\right)\cos\theta\right]^{1/2} \ll 1, \tag{26}$$

and restratification by FSI dominates convection. In general, given the surface forcing and frontal strength, Eq. (25) can be solved for h/H.

The scaling expression in Eq. (25) provides a useful test for FSI based on observed conditions. First, by measuring the PV or the balanced Richardson number, Ri_B, the SBL depth, H, can be identified. Then, using the surface forcing and geostrophic shear, Eq. (25) can be used to predict whether FSI will be active, and the qualitative structure of the vertical density profile. If $h/H \simeq 1$, FSI is not expected to be active, and the SBL should be unstratified. However, if $h/H < 1$, FSI is possible, and a stable stratification is expected to develop for $-h < z < -H$. In Section 3 we will use the predicted convective layer depth, h, and the observed density and velocity profiles to test for FSI in the GS.

3. Observational evidence of symmetric instability in the Gulf Stream

Diagnostics were performed on the high-resolution SeaSoar/ADCP observations collected as part of CLIMODE to probe for evidence of SI in the GS. The diagnostics entailed calculating the various instability criteria for SI, i.e. (13), (14), (21) and (23). The analyses were performed on two surveys denoted as surveys 2 and 3. Survey 2 was to the east near the location where flow detrains from the GS and enters the recirculation gyre and where the GS front is relatively weak. Survey 3 was to the west where the GS front is strong and has a prominent warm core (Fig. 2).

Representative cross-stream sections of density and PV for the two surveys are shown in Fig. 3(c) and (d). The PV was calculated assuming that cross-front variations in velocity and density are large compared to along-front variations. On both sections there are regions where the PV was negative. To determine if the dominant mode of instability in these regions was SI, ϕ_{Ri_B} was calculated. The parameter ϕ_{Ri_B} is especially sensitive to the stratification since it

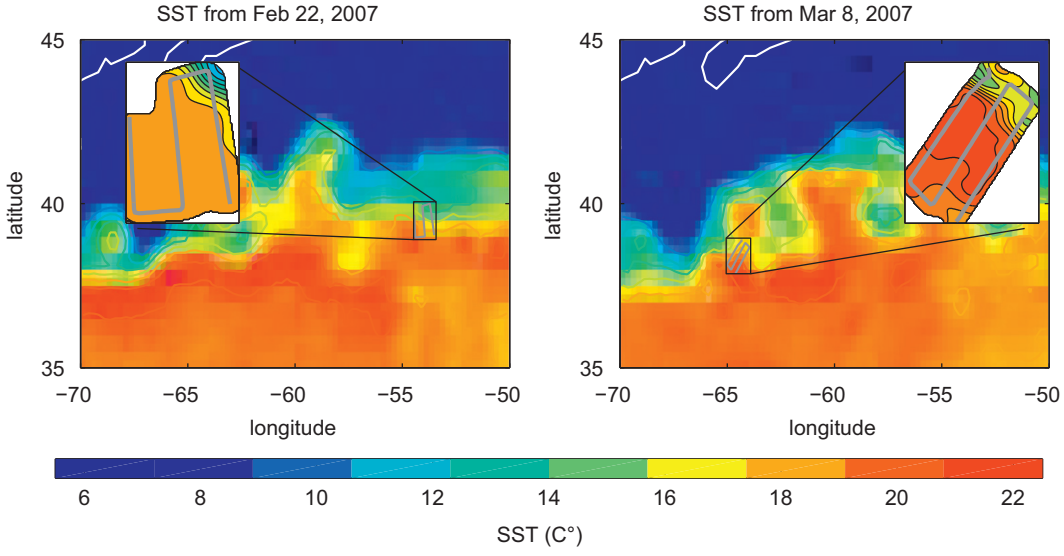

Fig. 2. Satellite-based SST around the time when survey 2 (left) and survey 3 (right) were made (the ship track is in gray). The insets in each figure show the near surface temperature as measured during the hydrographic surveys contoured every 1 °C. Line 2 of survey 2 corresponds to the middle section. Line 3 of survey 3 is the easternmost section.

Please cite this article as: Thomas, L.N., et al., Symmetric instability in the Gulf Stream. Deep-Sea Res. II (2013), http://dx.doi.org/10.1016/j.dsr2.2013.02.025

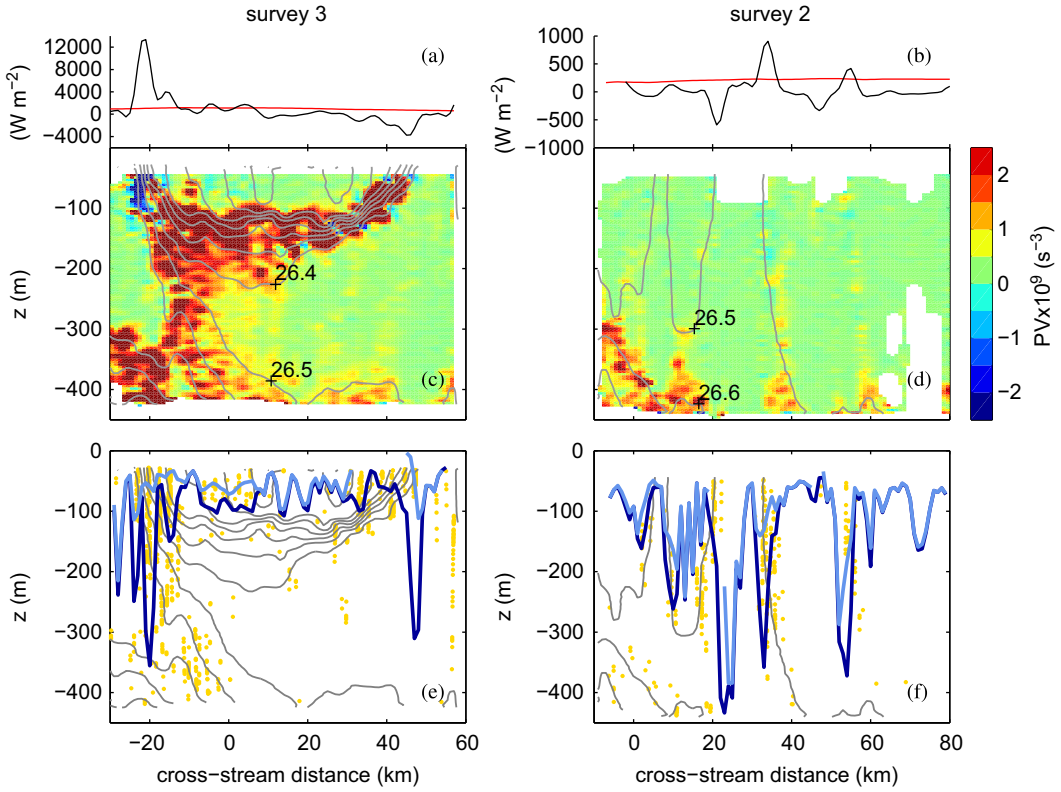

Fig. 3. Observational evidence of SI on survey 3, line 3 (left panels) and survey 2, line 2 (right panels). Panels (a) and (b): The cross-front structure of the heat loss (red) and Ekman buoyancy flux, expressed in units of a heat flux (black). Positive values of the EBF and heat flux indicate conditions favorable for FSI. Panels (c) and (d): Cross-stream sections of density (gray contours) and PV reveal regions where the PV was negative. As shown in panels (e) and (f), these regions tend to coincide with locations (denoted by the gold dots) where $-90^\circ < \phi_{Ri_B} < -45^\circ$ in regions of anticyclonic vorticity or $-90^\circ < \phi_{Ri_B} < \phi_c < -45^\circ$ in regions of cyclonic vorticity. They also lie in areas where the convective layer depth (cyan line) is less than the depth of the surface boundary layer (dark blue line) suggesting that the negative PV is associated with FSI. (For interpretation of the references to color in this figure legend, the reader is referred to the web version of this article.)

involves calculating N^{-2}, a quantity that can be quite large in the weakly stratified surface boundary layer. Thus to make as representative an estimate of N^2 as possible, ungridded profiles of density from the SeaSoar surveys were used to calculate the vertical density gradient at high-resolution. The gridded density fields were used to estimate $|\nabla_h b|^2$, which were then interpolated onto the cross-stream and vertical positions of the SeaSoar profiles to obtain high-resolution estimates of ϕ_{Ri_B}. Values of ϕ_{Ri_B} that satisfy criteria (13) and (14) were isolated and their locations are highlighted in Fig. 3(e) and (f). The collocation of waters with $q<0$ that satisfy criteria (13) and (14) on the sections indicates that the negative PV is associated with stable stratification, strong baroclinicity, and thus a symmetrically unstable flow.

As described in Section 2.3, mixing of PV by SI increases the PV of the boundary layer and hence stabilizes the flow unless the current is driven by buoyancy loss and/or an EBF that induce PV fluxes that satisfy (18). Shipboard meteorology was used to calculate the net heat flux and EBF. Profiles of the EBF and heat loss are shown in Fig. 3 (a) and (b). The atmospheric forcing was much stronger on survey 3, with wind-stress values ranging from 0.2 to 0.9 N m^{-2} and net heat fluxes of order 1000 W m^{-2}. The EBF was highly variable across survey 3, reflecting changes in the frontal structure. At the North Wall of the GS the EBF was more than an order of magnitude larger than surface heat flux, with a peak equivalent to 12,000 W m^{-2} of heat loss. Not surprisingly, under such strong destabilizing forcing the PV at the GS is negative down to over 100 m. While the forcing was weaker on survey 2, with a heat loss of a few hundred W m^{-2} and an EBF that did not exceed 1000 W m^{-2}, regions of negative PV correspond to peaks in the EBF, suggesting a causal link between the forcing and the observed PV distribution.

Apart from destabilizing forcing and a flow with negative PV, the condition for FSI to be the dominant mode of instability is for the convective layer to be shallower than the surface boundary layer. To test this criterion, the depths of both layers were estimated for each survey. The thickness of the surface boundary layer, H, was estimated using the bulk, balanced Richardson number criterion (22). The sum of the Ekman and surface buoyancy fluxes, the surface cross-front buoyancy gradient, and the surface boundary layer depth was used to estimate the convective layer depth, h, by solving (25). The depths of both layers are indicated in Fig. 3(e) and (f). On both surveys there are locations where h is significantly smaller than H. These regions tend to coincide with fronts where ϕ_{Ri_B} falls in the SI range (13) and (14) and the sum of the Ekman and surface buoyancy fluxes is positive, and thus where all three criteria for SI are satisfied. While these observations are suggestive of SI, the evidence is still somewhat circumstantial because more definitive measures of SI and the turbulence that it generates (such as the turbulent dissipation rate e.g. D'Asaro et al., 2011) were not collected on the surveys. To determine if the conditions observed in the GS were conducive for SI and to quantify the energy transfer associated with the instabilities that could have been present, a high resolution large eddy simulation (LES) was conducted with initial conditions and forcing representative of the observations.

4. Large eddy simulation of forced symmetric instability

The configuration of the LES, which is schematized in Fig. 4, is meant to be an idealized representation of the flow and forcing

Please cite this article as: Thomas, L.N., et al., Symmetric instability in the Gulf Stream. Deep-Sea Res. II (2013), http://dx.doi.org/10.1016/j.dsr2.2013.02.025

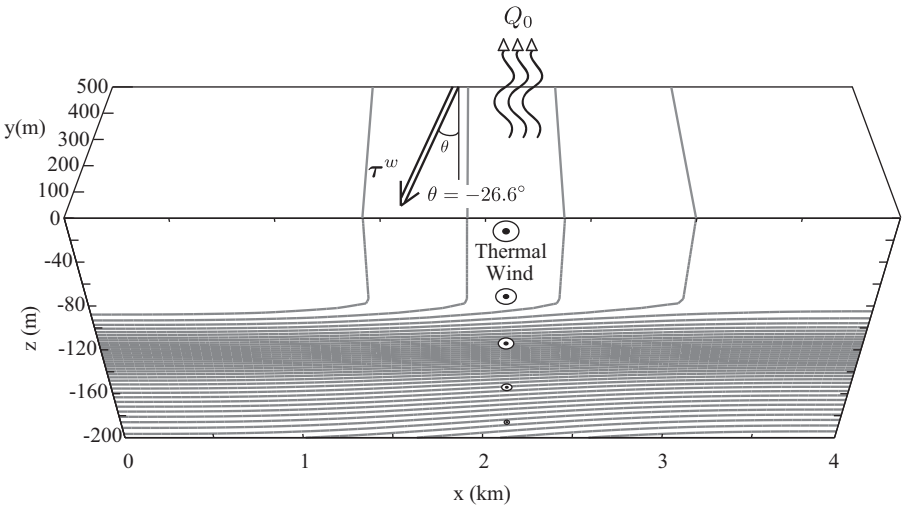

Fig. 4. Schematic of the LES configuration.

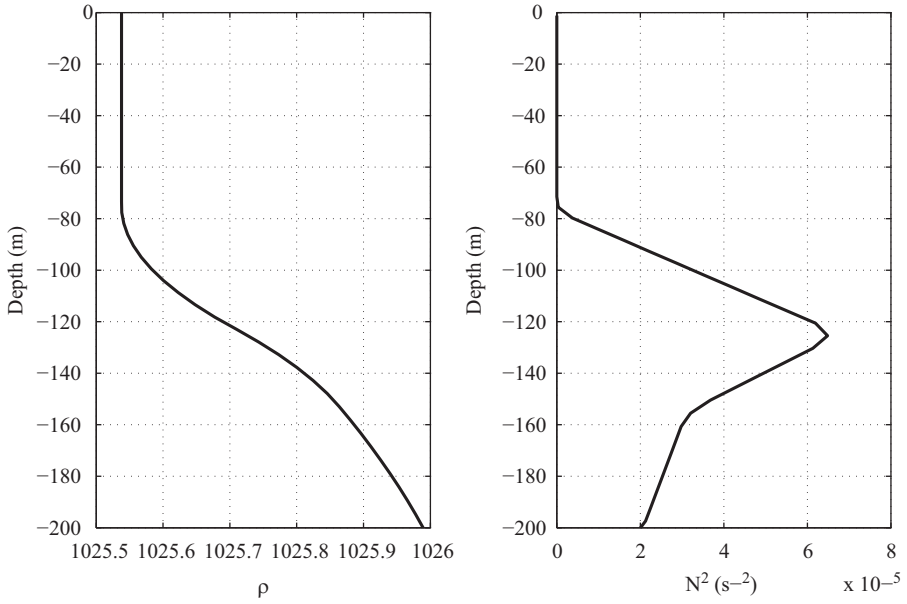

Fig. 5. Initial profiles of (left) density and (right) the buoyancy frequency squared for the large-eddy simulation described in Section 4.

along a subsection of survey 3, line 3. The initial stratification, lateral density gradient, and the surface forcing were based on averages of the observed fields from survey 3, line 3 collected between 0 and −15 km in the cross-stream direction (see the left hand panel of Fig. 3). More specifically, the density field was initialized using a piecewise linear buoyancy frequency, shown in Fig. 5, that captures key features of the observed stratification. The initial mixed layer depth is 73 m and stratification, $N_0^2(z)$, increases rapidly with depth below the mixed layer before reaching a maximum buoyancy frequency squared of 6.5×10^{-5} s^{-2} at a depth of 125 m. In order to speed the development of frontal circulations, we initialized the cross-front buoyancy field with a sinusoidal perturbation:

$$b(x,z,t=0) = \int N_0^2\, dz + M^2\left[x + \frac{LX}{2\pi}\sin\left(\frac{2\pi x}{LX}\right)\right]. \tag{27}$$

Although the strength of the front is not uniform across the domain, periodic boundary conditions can still be used after subtracting the background buoyancy gradient, M^2, from Eq. (27). The initial velocity field is in thermal wind balance with the buoyancy, so that $\partial v/\partial z = (\partial b/\partial x)/f$. A list of the forcing and flow parameters used in the simulation is given in Table 1.

Table 1
Parameters for the large-eddy simulation.

(*LX*,*LY*,*LZ*)	(*NX*,*NY*,*NZ*)	M^2	Q_0
(4 km, 500 m, 200 m)	(768, 96, 50)	-1.3×10^{-7} s^{-2}	1254 W/m^2
B_0	τ_x^w	τ_y^w	*EBF*
5.3×10^{-7} m^2/s^3	−0.20 N/m^2	−0.48 N/m^2	6.5×10^{-7} m^2/s^3

The numerical method utilized in the LES is the same as in the three-dimensional simulations reported in Taylor and Ferrari (2010) and Thomas and Taylor (2010) with periodic boundary conditions in both horizontal directions. Flux boundary conditions were implemented on the upper boundary, while a sponge layer was placed at the bottom of the computational domain from $-200\text{ m} < z < -175\text{ m}$ which relaxes the velocity and density towards the initial condition and reduces reflections of internal gravity waves. It is important to note that the computational domain size in the along-front direction is not large enough to capture baroclinic instability in the mixed layer. Based on the

Please cite this article as: Thomas, L.N., et al., Symmetric instability in the Gulf Stream. Deep-Sea Res. II (2013), http://dx.doi.org/10.1016/j.dsr2.2013.02.025

analysis by Stone (1970) and the parameters used here, the horizontal wavelength associated with the smallest baroclinically unstable mode is approximately 2.5 km, significantly larger than the along-front domain size of 500 m.

A visualization of the temperature and horizontal velocity from the LES is shown in Fig. 6 after three inertial periods. The temperature has been inferred from the LES density field by assuming a constant thermal expansion coefficient of $\alpha = 2.4 \times 10^{-4}\ ^{\circ}\mathrm{C}^{-1}$. At the time shown in Fig. 6, the strength of the front remains inhomogeneous across the domain with a relatively weak temperature gradient near the center of the domain and an outcropping front appearing on the left side of the figure. The stronger frontal region is also associated with a large along-front velocity which is only slightly reduced from the initial maximum value of $\max|V_g|(t=0) \simeq 0.56$ m/s.

The criteria introduced in Section 2.1 to identify regions with active SI can be tested using results from the LES. Since the LES has sufficient resolution to resolve turbulent overturns, Ri_B is very noisy when calculated at the grid scale. Instead, the vertical and horizontal buoyancy gradients, N^2 and M^2, were smoothed over 200 m in the horizontal directions before calculating Ri_B and ϕ_{Ri_B}. Fig. 7(a) shows ϕ_{Ri_B} as a function of cross-stream distance and depth for the same time as shown in Fig. 6. The depths of the convective and surface boundary layers (calculated with the same method used in the observational analysis) are also shown in the figure. Waters with unstable stratification and $\phi_{Ri_B} < -90^{\circ}$ tend to

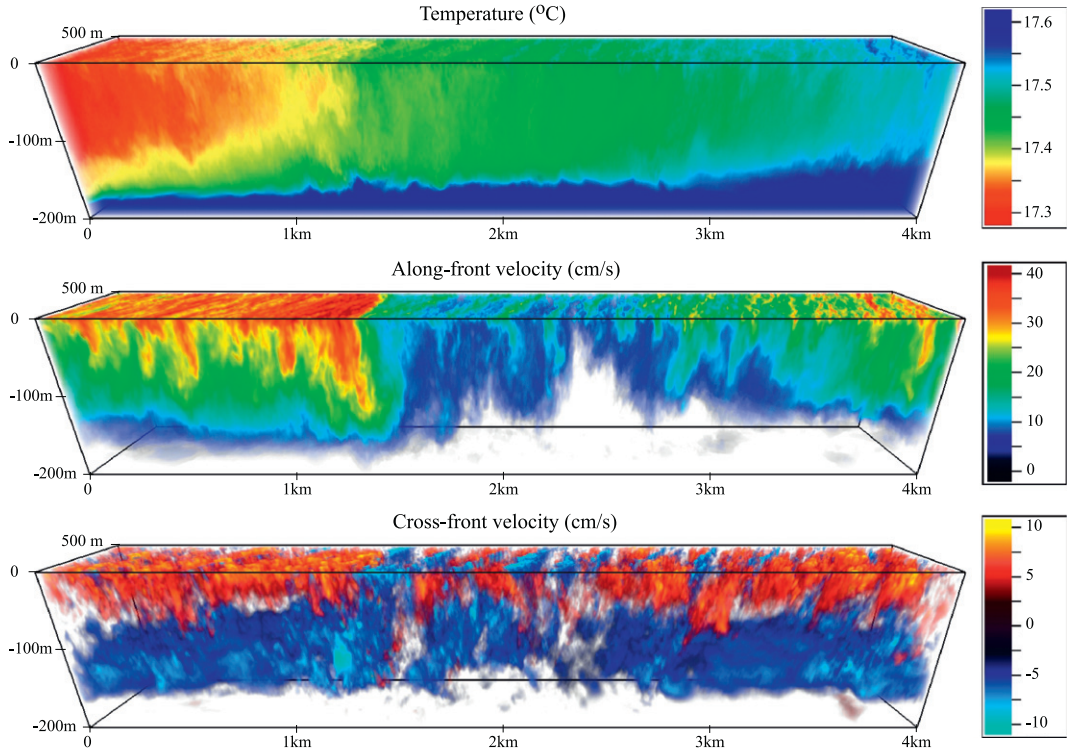

Fig. 6. Visualization of the temperature and horizontal velocity fields from the LES. In order to emphasize the regions with larger velocities, the volume visualization of both velocity components have been made transparent for $|u|, |v| < 2.5$ cm/s.

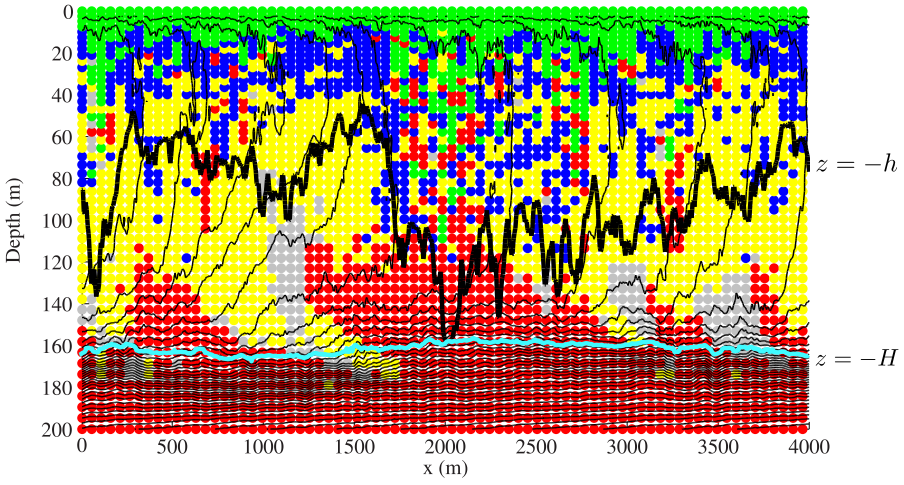

Fig. 7. Cross-front section of ϕ_{Ri_B} from the LES. The color scheme is the same as that used in Fig. 1. The depths of the convective layer (black) and surface boundary layer (cyan) are also indicated. (For interpretation of the references to color in this figure legend, the reader is referred to the web version of this article.)

Please cite this article as: Thomas, L.N., et al., Symmetric instability in the Gulf Stream. Deep-Sea Res. II (2013), http://dx.doi.org/10.1016/j.dsr2.2013.02.025

reside within the convective layer. There are also regions with stable stratification yet with flow that is unstable to SI ($-90^\circ < \phi_{Ri_B} < -45^\circ$). These are generally confined to depths where $-H < z < -h$. This tendency for symmetrically unstable flow to coincide with regions where there is a significant gap between the convective and surface boundary layers is also seen in the observations (Fig. 3).

A more quantitative comparison between the observations and the LES can be made by comparing representative profiles of the balanced Richardson number. This was done by calculating cross-stream means of N^2 and $|\nabla_h b|$, averaged along surfaces of constant z/H (denoted as $\langle N^2 \rangle$ and $\langle M^2 \rangle$, respectively) that were then used to compute a mean, balanced Richardson number, $\langle Ri_B \rangle \equiv \langle N^2 \rangle f^2 / \langle M^2 \rangle^2$. Observations from survey 3, line 3 collected between cross-stream distances of -15 km and 0 km were used in the comparison since the initial conditions and forcing of the LES were based on this data. The temporal evolution of $\langle Ri_B \rangle$ from the LES is illustrated in Fig. 8. Within three inertial periods and beneath the convective layer, the SBL transitions from being unstratified to stably stratified in spite of the destabilizing forcing, a consequence of the restratifying tendency of SI. In this relatively short period of time the profile of $\langle Ri_B \rangle$ approximately reaches a steady state, with a vertical structure that resembles the observations given the scatter in the data. This suggests that the bulk properties of the SBL seen in the observations are consistent with a flow undergoing FSI.

An important consequence of SI is that energy is extracted from a balanced front, converted to three-dimensional turbulent kinetic energy (TKE), and ultimately molecular dissipation. In order to determine the relative importance of this source of TKE to the boundary layer turbulence, we can compare the geostrophic shear production (GSP) with other sources of TKE. Fig. 9 shows several possible sources of TKE diagnosed from the LES. Near the surface, the wind stress generates TKE through the ageostrophic shear production (ASP) term, where

$$\mathrm{ASP} = -\overline{\mathbf{u}'w'} \cdot \left(\frac{\partial \mathbf{u}}{\partial z} - \frac{\partial \mathbf{u}_g}{\partial z} \right). \tag{28}$$

The ASP is large near the surface where it is nearly balanced by the dissipation, while its vertically averaged contribution is small as argued by Taylor and Ferrari (2010). The two remaining terms which contribute to the vertically integrated TKE production are the buoyancy flux, $\overline{b'w'}$, and the GSP. Positive values of the buoyancy flux indicate convective conditions, which in this case are caused by a combination of the unstable surface buoyancy flux, B_0, and the Ekman buoyancy flux (EBF). Although the buoyancy flux is a significant source of TKE due to the strong forcing conditions, the GSP is even larger, especially in the lower half of the low PV layer where it dominates the TKE production. This implies that the extraction of frontal kinetic energy may be an important source of turbulence in the GS.

We can use these results from the LES to develop a parameterization for the GSP. To begin, we invoke the theoretical scaling of Taylor and Ferrari (2010) that the sum of the GSP and BFLUX is a linear function of depth:

$$\mathrm{GSP} + \mathrm{BFLUX} \approx (\mathrm{EBF} + B_o)\left(\frac{z+H}{H}\right). \tag{29}$$

By writing an approximate expression for the buoyancy flux profile, we can use Eq. (29) to derive an expression for the GSP. Assuming that the buoyancy flux is a linear function of depth inside the convective layer, and zero below

$$\mathrm{BFLUX} \approx \begin{cases} \overline{b'w'} \approx B_o(z+h)/h, & z > -h, \\ 0, & z < -h, \end{cases} \tag{30}$$

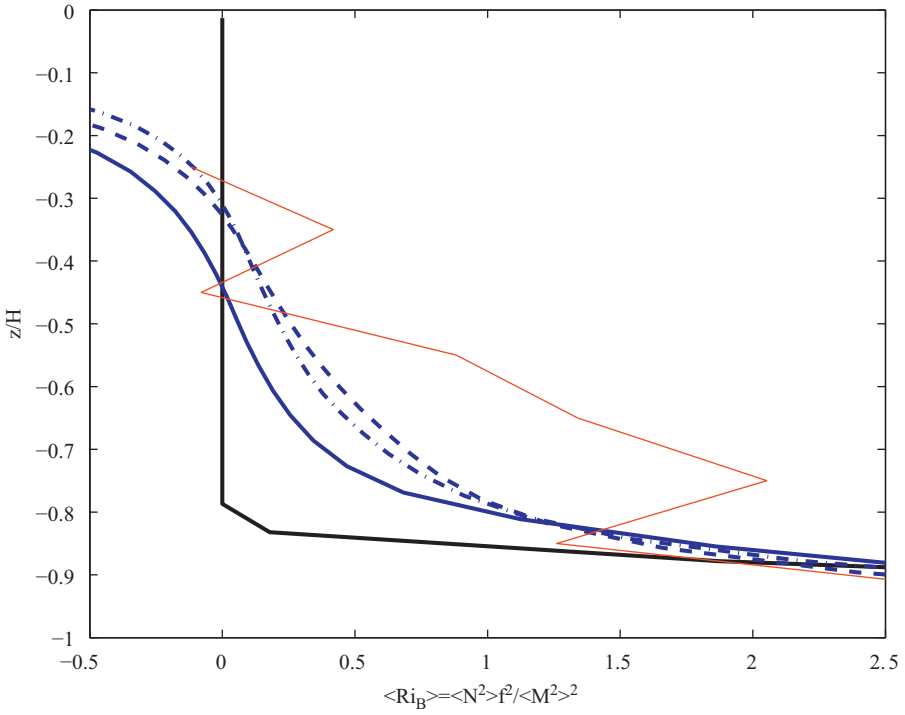

Fig. 8. The Richardson number of the balanced flow laterally averaged along surfaces of constant z/H, $\langle Ri_B \rangle$, from line 3, survey 3 for cross-stream distances between -15 km and 0 km (red). For comparison, profiles are shown of $\langle Ri_B \rangle$ from the LES averaged across the entire computational domain and over four time periods: $t=0$ (black), $0 < t < 2\pi/f$ (blue solid), $2\pi/f < t < 4\pi/f$ (blue dashed), and $4\pi/f < t < 6\pi/f$ (blue dashed–dotted). (For interpretation of the references to color in this figure legend, the reader is referred to the web version of this article.)

Please cite this article as: Thomas, L.N., et al., Symmetric instability in the Gulf Stream. Deep-Sea Res. II (2013), http://dx.doi.org/10.1016/j.dsr2.2013.02.025

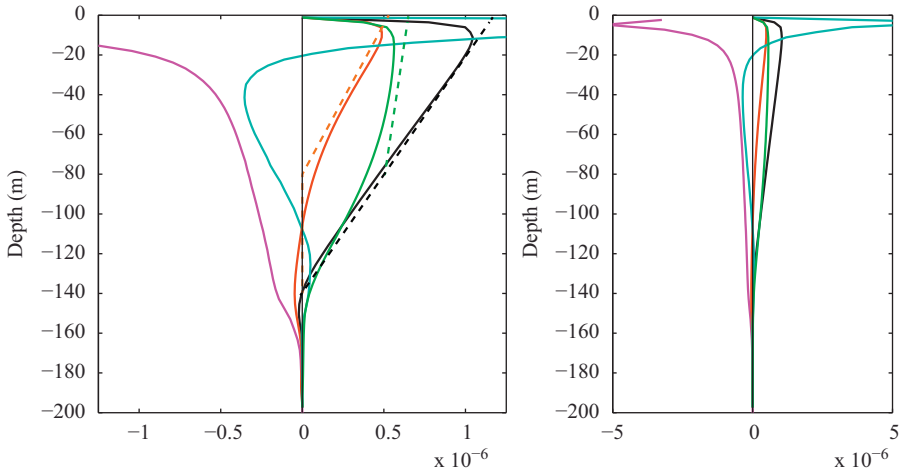

Fig. 9. TKE production terms from the LES (right panel), namely the geostrophic shear production (GSP, solid green), buoyancy flux (BFLUX, solid red), and their sum (solid black), along with the ageostrophic shear production (ASP, cyan) and minus the dissipation (magenta). Each term is averaged over the horizontal domain and for one inertial period. Parameterizations for the buoyancy flux (red dashed), the GSP (green dashed), and their sum (black dashed) based on Eqs. (29)–(31) are shown for comparison in the panel on the left which is an expanded view of the panel on the right. All quantities are in units of W kg^{-1}. (For interpretation of the references to color in this figure legend, the reader is referred to the web version of this article.)

the GSP can be parameterized with the following expression:

$$\mathrm{GSP} \approx \begin{cases} (\mathrm{EBF}+B_o)\left(\dfrac{z+H}{H}\right)-B_o\left(\dfrac{z+h}{h}\right), & z>-h, \\ (\mathrm{EBF}+B_o)\left(\dfrac{z+H}{H}\right), & -H<z<-h, \\ 0, & z<-H. \end{cases} \tag{31}$$

The parameterizations for the buoyancy flux, GSP, and their sum compare favorably to the LES results both in their vertical structure and amplitude (Fig. 9).

5. Sources and sinks of kinetic energy in the Gulf Stream

The submesoscale and mesoscale currents that make up the Gulf Stream gain KE primarily through the release of available potential energy. As described above, these baroclinic currents are potentially susceptible to SI which can act as a sink of KE. In this section we attempt to quantify these sinks and sources of KE using the observations.

5.1. Removal of kinetic energy from the Gulf Stream by symmetric instability

It is thought that western boundary currents such as the GS lose their KE primarily through bottom friction at the western boundary. The extraction of KE by SI in the surface boundary layer of western boundary currents is a break from this paradigm. We will estimate this KE sink by calculating the net dissipation associated with SI using the shipboard meteorology and SeaSoar hydrography and the parameterization for the GSP (31). We will also characterize the conditions that result in high frontal dissipation.

Dissipation by SI will be particularly large at strong lateral density gradients forced by down-front winds where the EBF is large. Thus, a collocation of frontogenetic strain and an alignment of the winds with a frontal jet will conspire to give very large KE extraction by SI. A horizontal flow with frontogenetic strain results in an increase in the lateral buoyancy gradient at a rate given by the *frontogenesis function*

$$F_{front} \equiv 2\mathbf{Q}\cdot\nabla_h b = \frac{D}{Dt}\left|\nabla_h b\right|^2, \tag{32}$$

where

$$\mathbf{Q} = \left(-\frac{\partial \mathbf{u}}{\partial x}\cdot\nabla_h b, -\frac{\partial \mathbf{u}}{\partial y}\cdot\nabla_h b\right) \tag{33}$$

is the so-called *Q-vector* (Hoskins, 1982). The frontogenesis function was evaluated on survey 3 using only the geostrophic component of the velocity in Eq. (33). The geostrophic velocity was inferred using density and velocity observations and constraining $\mathbf{u}_g$ to satisfy the thermal wind balance and to be horizontally non-divergent following the method of Rudnick (1996).[1]

The near-surface distribution of F_{front} is shown in Fig. 10(a). Strong frontogenesis ($F_{front} \sim 1\times10^{-17}$ s^{-5}) occurs in the North Wall of the GS near the top of line 3 of the survey. To put this value in perspective, as fluid parcels transit the region of frontogenetic strain where $F_{front} \sim 1\times10^{-17}$ s^{-5}, which is around 25 km wide, moving at ~ 1 m s^{-1} (a speed representative of the GS in the North Wall) their horizontal buoyancy gradient would increase by 5×10^{-7} s^{-2}.

Previous studies have found that frontogenesis also occurs on a smaller scale driven by wind-forced ageostrophic motions (Taylor and Ferrari, 2010; Thomas and Lee, 2005; Thomas and Taylor, 2010) and in the LES described above, the frontogenesis driven by SI rivals that associated with the geostrophic flow estimated from the observations. Frontogenetic circulation can be seen in the visualization shown in Fig. 6 as a convergent cross-front velocity at the surface near the region with the strongest temperature gradient. A cross-section of the frontogenesis function, evaluated from the LES is shown in Fig. 10(b). Note that here, the full velocity has been used in evaluating the frontogenesis function instead of just the geostrophic component. The frontogenesis function is very large near the surface at the strongest front at $x \simeq 1.5$ km, indicating that the frontogenetic strain fields in the LES and observations are comparable in magnitude.

In addition to the intense frontogenesis inferred from the observations, the wind-stress is down-front and large in magnitude (e.g. 10(a)). Both of these conditions conspired to amplify the

[1] The velocity and density fields used in the calculation were objectively mapped using the method of Le Traon (1990). Each field minus a quadratic fit was mapped at each depth using 5% noise and an anisotropic Gaussian covariance function with e-folding lengths of 20 and 10 km in the along- and cross-stream directions, respectively.

Please cite this article as: Thomas, L.N., et al., Symmetric instability in the Gulf Stream. Deep-Sea Res. II (2013), http://dx.doi.org/10.1016/j.dsr2.2013.02.025

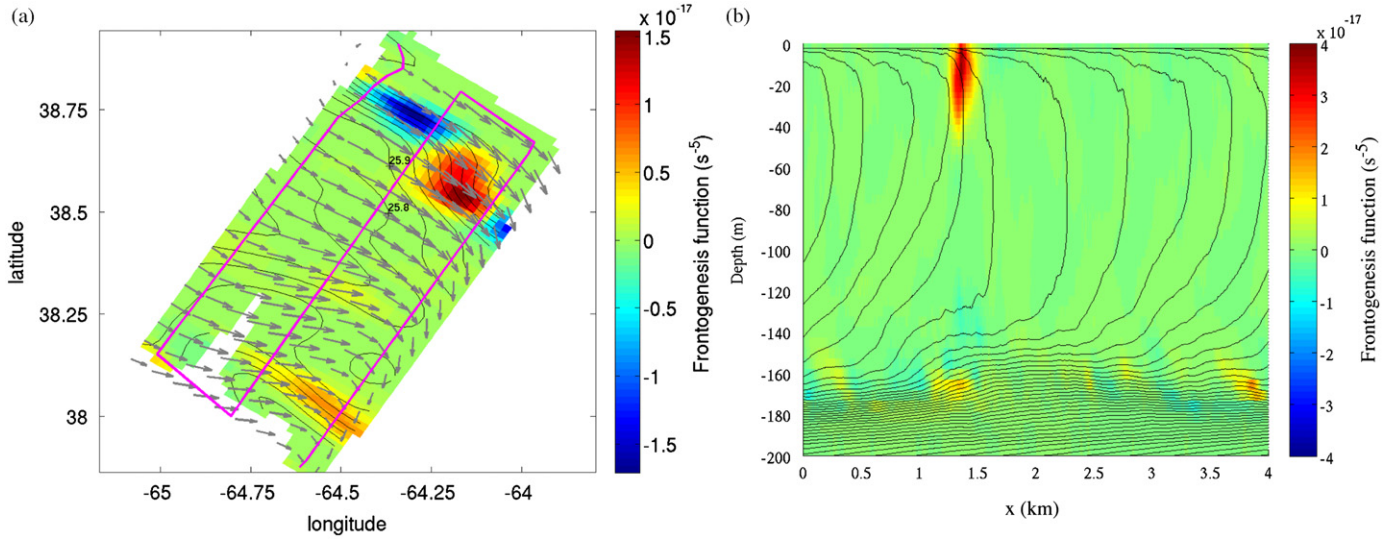

Fig. 10. (a) The density (contours) and frontogenesis function (shades) at $z=-44$ m on survey 3. Vectors represent the wind-stress (for scaling, the maximum magnitude of the wind-stress is 0.94 N m^{-2} on the survey). The magenta line is the ship track. Line 3 is the easternmost line of the survey. (b) A cross-section of the density (contours) and frontogenesis function averaged over six hours (shades) from the LES. Since spatial gradients are very large on the scale of three-dimensional turbulence, the velocity and buoyancy gradients appearing in the frontogenesis function were each averaged across the along-front direction and smoothed in the along-front direction over a window of 250 m. (For interpretation of the references to color in this figure legend, the reader is referred to the web version of this article.)

EBF at the North Wall, resulting in the peak value equivalent to 12,000 W m^{-2} of heat loss seen in Fig. 3(a). On the South Wall of the warm core, the flow is also frontogenetic but the winds are up-front and are not conducive for driving SI. Upfront winds act to restratify the water column, increasing the PV, which tends to suppress SI and its associated extraction of KE. Therefore when averaged laterally over an area where the winds are both up- and down-front, SI will result in a net removal of KE from the frontal circulation.

The rate of KE removal by SI was estimated by averaging the parameterization for the GSP (31) over the area spanned by survey 3. As shown in Fig. 11, the average GSP peaks at the surface and decays with depth, extending to over 250 m, a depth set by the thick SBLs near the North Wall (e.g. Fig. 3(a)). Integrated over depth the average GSP (multiplied by density) amounts to 33 mW m^{-2}. The contribution to the GSP from wind-forcing alone is assessed by setting $B_o=0$ in (31). Wind forcing results in a depth integrated GSP of 27 mW m^{-2}, suggesting that down-front winds are the dominant trigger for SI on this survey.

On survey 2, both the fronts and atmospheric forcing were weaker (e.g. Fig. 3), which would imply weaker SI and a reduced GSP. Indeed the parameterization for the GSP (31) averaged over survey 2 is over an order of magnitude smaller than that on survey 3 (compare Figs. 14 and 11). Integrated over depth, the net GSP is 1 mW m^{-2}, which is close to the value for wind-forcing alone, namely 0.9 mW m^{-2}.

5.2. Removal of available potential energy from the Gulf Stream by baroclinic instability

While SI can draw KE directly from the GS, the current also loses available potential energy (APE) to BCI. The GS's APE loss translates to a KE gain for BCI at a rate given by the buoyancy flux

$$I=\overline{w'b'}^{xy} \tag{34}$$

(where the overline denotes a lateral average over the area of the survey and primes the deviation from that average). We attempt to quantify this source of KE by calculating the the buoyancy flux following a method similar to that employed by Naveira Garabato et al. (2001) of using a vertical velocity field inferred by solving the omega equation

$$f^2\frac{\partial^2 w}{\partial z^2}+N^2\nabla_h^2 w=2\nabla\cdot\mathbf{Q}_g, \tag{35}$$

here written in its quasi-geostrophic form where ∇_h^2 is the horizontal Laplacian and the subscript "g" indicates that the Q-vector in (35) is evaluated using the geostrophic velocity (Hoskins et al., 1978).

The omega equation was solved for survey 3 with w set to zero at the boundaries of the domain over which the computation was made. Setting $w=0$ at the bottom of the domain is somewhat of an arbitrary constraint often used in studies of frontal vertical circulation that can affect the solution away from the boundaries (e.g. Allen and Smeed, 1996; Pollard and Regier, 1992; Rudnick, 1996; Thomas et al., 2010). Therefore, it is critical to push the bottom of the domain as far from the region of interest as possible so that the inferred w is not greatly affected by the boundary condition. Therefore, the computational domain for the omega equation calculation was extended beneath the SeaSoar survey down to 1000 m. Deep CTD casts taken as part of CLIMODE were used to estimate N^2 beneath the SeaSoar survey, and the Q-vector was set to zero at these depths. The divergence of the Q-vector is largest in magnitude near the surface where frontogenesis is most intense. Thus setting $\mathbf{Q}_g=0$ at depths beneath the SeaSoar survey does not greatly affect the solution to (35) in the near-surface region of interest.

Plan view and cross-stream sections of w for survey 3 are shown in Figs. 12 and 13. As to be expected, in regions of frontogenesis the vertical circulation is thermally direct, with downwelling and upwelling on the dense and less dense sides of the front, respectively. The strong frontogenetic strain where line 3 intersects the Northern Wall of the GS results in a downdraft with a magnitude of over 100 m day^{-1} that extends through the $\sim$300 m SBL to the north of the GS. This downdraft is coincident with the plume of low PV and high fluorescence evident in Figs. 3(c) and 13. Conversely, regions of upwelling correspond to areas of low fluorescence and high PV (e.g. near -10 km in the cross-stream direction). The correlation between the fluorescence, PV, and w suggests that three-dimensional processes such as baroclinic instability play a key role in the vertical exchange of

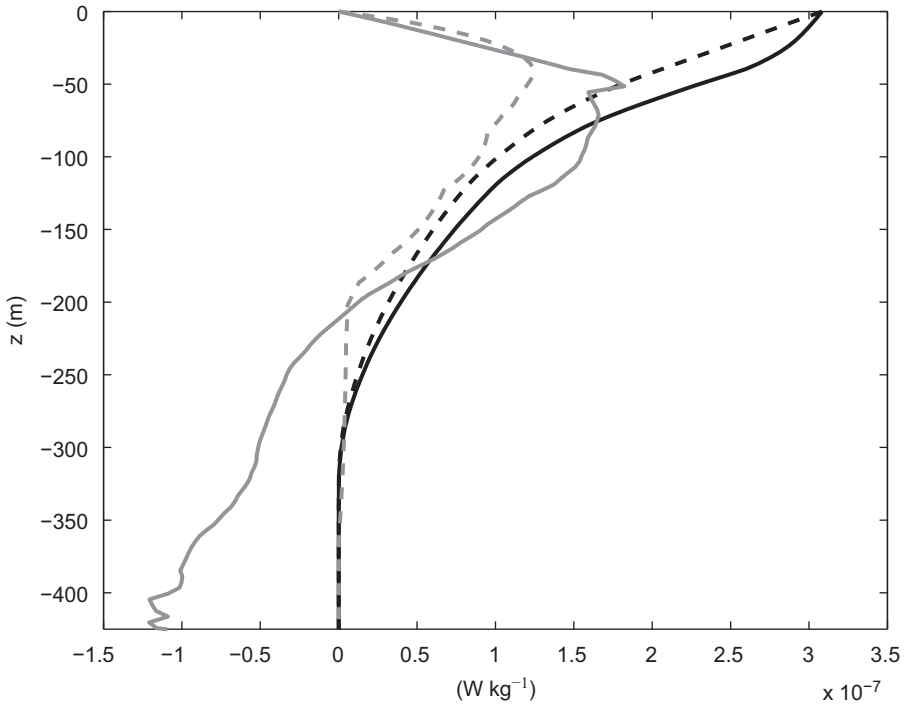

Fig. 11. An estimate for SI's geostrophic shear production, e.g. (31), attributed to both wind-forcing and cooling (black) and wind-forcing alone (black dashed) for survey 3. Also shown is the buoyancy flux associated with baroclinic instability estimated using the omega equation diagnostic, $\overline{w'b'}^{xy}$ (gray) and the parameterization for BCI (36) (gray dashed). All quantities have been averaged laterally over the survey.

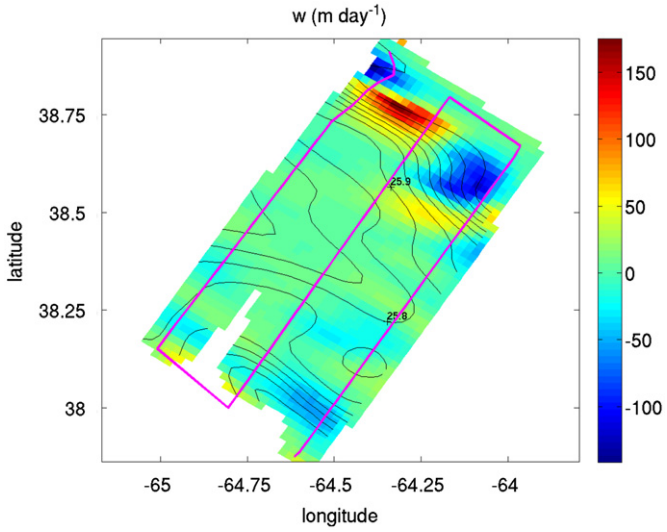

Fig. 12. The density (contours) and inferred vertical velocity (shading) at $z=-44$ m on survey 3 calculated using the quasigeostrophic omega equation.

biomass and PV across the pycnocline. As described in Joyce et al. (2009), a similar correlation between low PV, enhanced fluorescence, and high oxygen was observed on survey 2.

Using the solution to the omega equation, the buoyancy flux (34) was estimated across the area spanned by survey 3 (e.g. Fig. 11). Above $z\approx-200$ m, $\overline{w'b'}^{xy}$ is positive, implying that APE is being extracted from the GS over this range of depths. The buoyancy flux peaks near $z\approx-50$ m which is within the SBL (e.g. Fig. 3(a)). While the positive buoyancy flux is suggestive of BCI, other process that drive a net thermally direct circulation (such as large-scale frontogenetic strain) could have been present as well.

To determine whether the buoyancy flux estimated using the omega equation is consistent with the energetics of BCI, the buoyancy flux associated with BCI was inferred using the parameterization of Fox-Kemper et al. (2008)

$$\overline{w'_{BCI}b'_{BCI}}^{x}=\frac{C_e(\overline{H}^{x})^2|\overline{\nabla_h b}^{xz}|^2}{|f|}\mu(z) \tag{36}$$

where $\overline{()}^{z}$ and $\overline{()}^{x}$ indicates an average across the SBL and in the along-front direction, respectively, $C_e\approx0.06$ is an empirically determined coefficient, and $\mu(z)$ is a vertical structure function that goes to zero at the top and bottom of the SBL. The parameterization (36) captures the vertical mode of BCI confined to the SBL associated with submesoscale mixed layer eddies (MLEs) (Boccaletti et al., 2007; Fox-Kemper et al., 2008). Low vertical mode BCIs with a deeper extension could also contribute to the buoyancy flux but are not parameterized by (36).

The density field averaged in the along-stream direction was used to evaluate (36). The cross-stream average of $\overline{w'_{BCI}b'_{BCI}}^{x}$ has similar features to $\overline{w'b'}^{xy}$ in the upper 200 m (Fig. 11). The zero crossing of the buoyancy flux assessed using the vertical velocities from the omega equation is close to the depth where $\overline{w'_{BCI}b'_{BCI}}^{x}$ averaged across the survey goes to zero. The two buoyancy fluxes have maxima near 50 m that are of similar strength. Given the potential errors that could arise in calculating the correlation between w and b over a survey that spans only a few submesoscale meanders of the GS, the agreement between the two estimates for the buoyancy flux suggests that the inferred APE release in the upper 200 m of the GS is qualitatively consistent with the energetics of baroclinic instability. When integrated over this depth range, the net buoyancy flux (multiplied by density) is estimated as 23 mW m^{-2} and 15 mW m^{-2} using (34) and (36), respectively. These values are smaller yet similar to the net GSP associated with SI.

On survey 2 an estimate of the APE release by BCI using the omega equation diagnostic could not be performed due to gaps in

Please cite this article as: Thomas, L.N., et al., Symmetric instability in the Gulf Stream. Deep-Sea Res. II (2013), http://dx.doi.org/10.1016/j.dsr2.2013.02.025

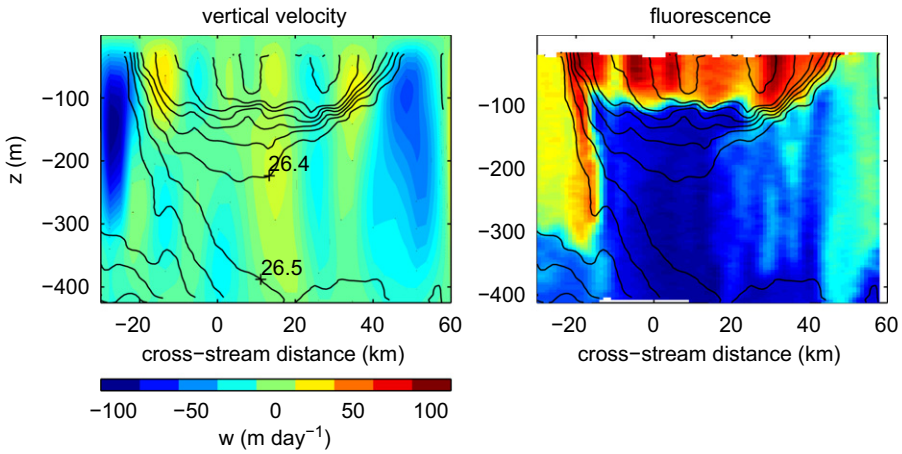

Fig. 13. The density (contours), inferred vertical velocity (left), and fluorescence (right) on line 3 of survey 3.

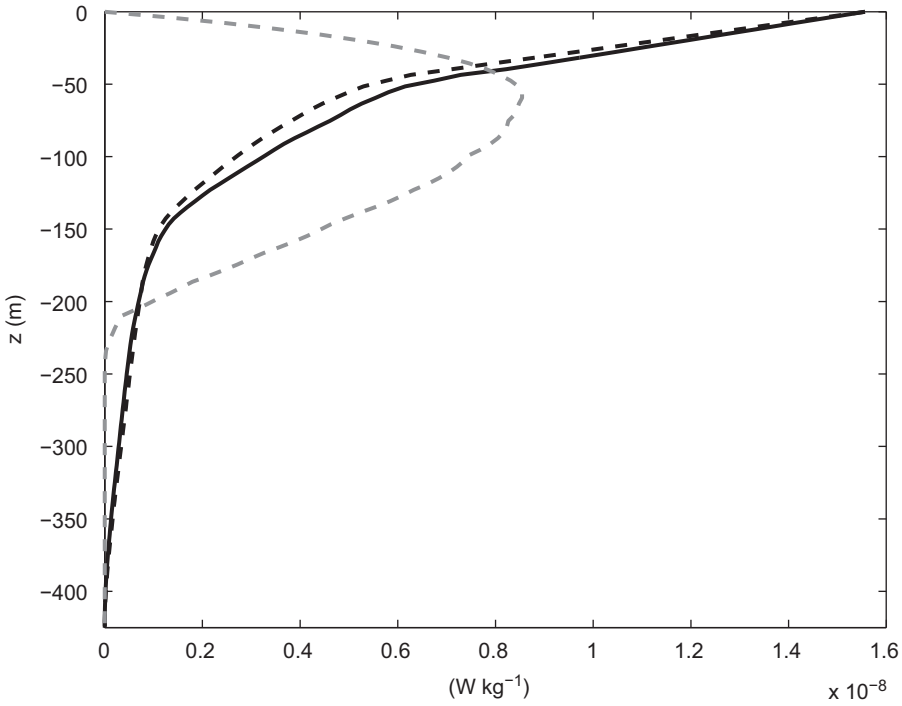

Fig. 14. An estimate for SI's geostrophic shear production, e.g. (31), attributed to both wind-forcing and cooling (black) and wind-forcing alone (black dashed) for survey 2. Also shown is the buoyancy flux associated with baroclinic instability estimated using the parameterization for BCI (36) (gray dashed). All quantities have been averaged laterally over the survey.

the velocity data and the relatively coarse along-front resolution of the survey. However, the buoyancy flux associated with BCI could be assessed using the parameterization (36). In spite of the deeper SBLs, owing to the weaker fronts of survey 2, $\overline{w'_{BCI}b'_{BCI}}^{x}$ is over an order of magnitude weaker than that estimated for survey 3 (Fig. 14). The parameterization suggests that the net APE release by BCI amounts to 1 mW m^{-2}, equivalent to the inferred net dissipation by SI on the survey. Therefore based on these observations we can conclude that under the strong wintertime forcing experienced on the surveys, SI plays a comparable role to BCI in the energetics of the GS.

6. Conclusions

High resolution hydrographic and velocity surveys of the Gulf Stream made during strong wintertime forcing evidence a symmetrically unstable current with negative PV caused by cooling and down-front winds. In spite of the large wintertime heat loss, a combination of frontogenetic strain associated with the geostrophic flow combined with down-front winds conspired to make the winds, through the Ekman advection of buoyancy, the dominant cause for the decrease in PV. The lowest PV observed in the surveys is found on the EDW isopycnal layer where it outcrops at the North Wall of the GS under the maximum in the EBF.

These observations may shed light on the question as to why EDW forms on the isopycnal layer bounded by the 26.4 and 26.5 kg m^{-3} density surfaces. The observations reveal that in the winter it is these density surfaces that outcrop in the North Wall of the GS where the horizontal density gradient of the open-ocean Northwest Atlantic is persistently strong (Belkin et al., 2009). Combined with a down-front wind, the outcrop of EDW isopycnal layer in the North Wall also coincides with a maximum in frictional PV removal which causes the PV to be preferentially reduced on this layer. This is indeed what is observed on survey 3.

Please cite this article as: Thomas, L.N., et al., Symmetric instability in the Gulf Stream. Deep-Sea Res. II (2013), http://dx.doi.org/10.1016/j.dsr2.2013.02.025

While frictional PV fluxes can locally dominate over diabatic PV fluxes along the fronts of the GS, PV budgets for the EDW isopycnal layer calculated using a coarse-resolution, data-assimilating numerical simulation suggest that when integrated over the entire outcrop area, heat loss rather than friction is the primary mechanism for the seasonal reduction of the volume integrated PV on the layer (Maze and Marshall, 2011). This does not necessarily imply that frontal processes are unimportant for EDW formation. Cooling dominates the PV budgets because it covers a larger outcrop area than wind-driven frictional PV fluxes. The large outcrop areas are to a large degree a reflection of the subsurface structure of the stratification and low PV anomalies that precondition the fluid for deep convective mixed layers. Thus processes that lead to the generation and subduction of water with anomalously low PV, such as those observed on the North Wall of the GS described here and in Thomas and Joyce (2010), can contribute indirectly to the formation of EDW and thus select the isopycnal layer on which it is found.

A large eddy simulation configured with flow and forcing parameters based on the observations reveals that the destabilizing winds and buoyancy loss generate a deepening SBL with negative PV yet with stable stratification across a large fraction of its thickness. The turbulence in this stratified layer derives its energy from both the buoyancy field and the geostrophic flow. In the LES the rate of KE extraction from the geostrophic flow by the turbulence scales with the EBF and surface buoyancy flux, in agreement with a simple parameterization for SI. While PV is well mixed in the SBL, buoyancy, momentum, and tracers retained significant vertical structure in spite of strong turbulence, with dissipation rates exceeding 1×10^{-6} W kg^{-1}.

These results have important implications for the parameterization of turbulent mixing in the upper ocean. The traditional view is that turbulence near the sea surface is driven solely by atmospheric forcing (winds or buoyancy fluxes). Our analysis shows that turbulence can also be generated through frontal instabilities. In addition, current parameterizations take a one-dimensional view where vertical mixing spans a boundary layer whose depth is commonly computed using a bulk Richardson number criterion (e.g. the KPP mixing scheme of Large et al., 1994 and the PWP model of Price et al., 1986). The critical bulk Richardson number used to determine the boundary layer depth is typically less than one, i.e. lower than the threshold for SI. Consequently, at a front undergoing SI these mixing schemes will underpredict the depth of the boundary layer. A second, and perhaps more important problem is that many models based on bulk criteria either assume uniform water mass properties in the boundary layer, or assign a very large vertical diffusivity. However, in observations taken during CLIMODE and the LES, vertical gradients of buoyancy, momentum, and tracers persist in the symmetrically unstable boundary layer. Vertical mixing is not strong enough to maintain a homogeneous boundary layer in the face of restratification. As shown by Taylor and Ferrari (2011) this has important consequences for the biology as well as the physics of the upper ocean, especially in the high latitudes where the strength of vertical mixing can determine the mean light exposure and hence growth rate of phytoplankton.

Apart from evidencing SI, the observational surveys of the GS show signs of baroclinic instability, namely thermally-direct vertical circulations that release available potential energy and advect tracers such as biomass and PV. These signatures of baroclinic instability are strongest in the surface boundary layer and are characterized by submesoscale length scales, suggesting that the instabilities are a form of the mixed layer eddies (MLEs) modeled by Boccaletti et al. (2007) and Fox-Kemper et al. (2008). While baroclinic instability injects kinetic energy into the geostrophic flow, symmetric instability extracts KE, transferring it to small scales where it can be dissipated by friction (Thomas and Taylor, 2010). The observations suggest that the rates of KE removal and injection by the two instabilities averaged over the surface boundary layer are of the same order of magnitude. This result implies that SI can limit or prevent the inverse cascade of KE by MLEs and points to an energy pathway where the Gulf Stream's reservoir of APE is drained by MLEs, converted to KE, then dissipated by SI and its secondary instabilities. It follows that this energy pathway would be preferentially opened during the winter, when strong atmospheric forcing both deepens the SBL, which allows for energetic MLEs to develop, and reduces the PV in frontal regions, triggering SI.

The depth-integrated dissipation associated with SI inferred from surveys 2 and 3 was 1 mW m^{-2} and 33 mW m^{-2}, respectively. This range of net dissipation is similar to that observed in the abyss of the Southern Ocean, $\mathcal{O}(1)$–$\mathcal{O}(10)$ m W m^{-2}, which has been ascribed to the breaking of internal waves generated by geostrophic currents flowing over rough topography, a process thought to remove about 10% of the energy supplied by winds to the global circulation (Naveira Garabato et al., 2004; Nikurashin and Ferrari, 2010). In contrast to breaking of internal waves however, dissipation associated with SI in the SBL is likely to exhibit a seasonal cycle and thus, averaged annually, will result in weaker net dissipation values. Having said this, recent observations in the Kuroshio taken during late spring have revealed local net dissipation rates of $\sim$100 m W m^{-2} at a symmetrically unstable front driven by weak atmospheric forcing, with minimal buoyancy loss and wind-stress magnitudes of less than 0.2 N m^{-2} (D'Asaro et al., 2011). The intense dissipation at the Kuroshio was attributable to the combination of an extremely sharp front and the down-front orientation of the wind which resulted in an EBF large enough to explain the observed dissipation. Thus SI and the KE extraction it induces is not solely a wintertime phenomenon, however, it is confined to frontal regions, which are limited in area. The contribution of dissipation associated with SI to the removal of KE from the entire ocean circulation is a challenging number to constrain owing to the dependence of SI on submesoscale frontal features. However, the wintertime observations from the GS described here suggest that this contribution could be significant, and thus future studies should aim to quantify it.

Acknowledgments

Thanks are due to all the colleagues in the CLIMODE project, especially those organizing this special issue and Frank Bahr at WHOI for his efforts in collecting the hydrographic and velocity measurements with the SeaSoar and shipboard ADCP. Support came from the National Science Foundation Grants OCE-0961714 (L.N.T.) and OCE-0959387 (T.M.J.) and the Office of Naval Research Grants N00014-09-1-0202 (L.N.T.) and N00014-08-1-1060 (J.R.T. and R.F.).

Appendix. Simple model for gravitational, inertial, and symmetric instability and their energy sources

The simplest model for studying the overturning instabilities that develop when $fq<0$ consists of a background flow with spatially uniform gradients: $u_g=(M^2/f)z-[(F^2-f^2)/f]y$, where M^2/f is the thermal wind shear and $F^2/f=f-\partial u_g/\partial y$ is the absolute vorticity of the geostrophic flow, both of which are assumed to be constant. The stratification, N^2, is also spatially uniform and has a value such that the PV of the geostrophic flow, $q=(F^2N^2-M^4)/f$ takes the opposite sign of f. The governing equation for the overturning streamfunction of the instabilities

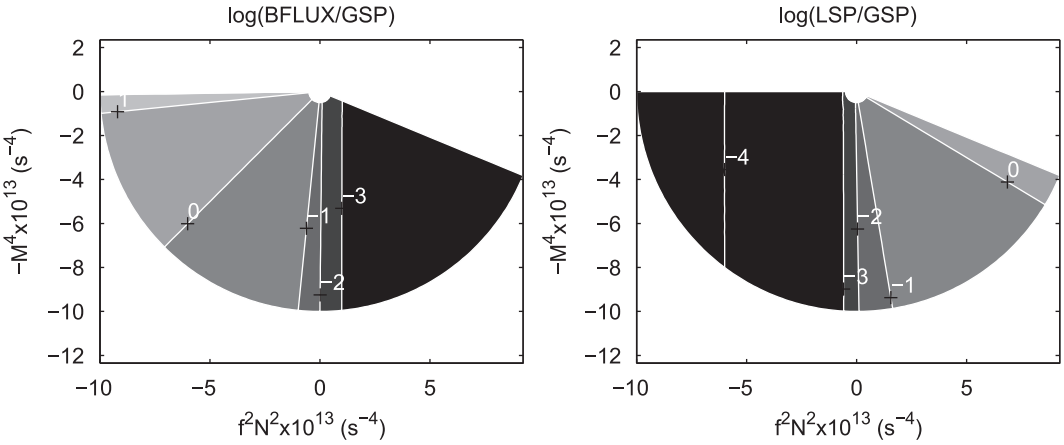

Fig. 15. Logarithm (base 10) of the ratio of the energy source terms for gravitational instability, SI, and inertial instability, i.e. (41) and (42), for the fastest growing mode that forms in a background flow with uniform vertical shear of strength M^2/f and absolute vorticity $F^2/f = 0.4f$, and stratification N^2. In the plots the angle measured counter-clockwise from the abscissa is ϕ_{Ri_B}. Given the anticyclonic vorticity of the flow, the value of ϕ_{Ri_B} below which the PV turns negative is $\phi_c = -21.8^\circ$.

(which are assumed to be invariant in the x-direction and of small amplitude so that their dynamics is linear) is

$$\frac{\partial^2}{\partial t^2}\left(\frac{\partial^2}{\partial y^2}+\frac{\partial^2}{\partial z^2}\right)\psi + F^2\frac{\partial^2\psi}{\partial z^2} + 2M^2\frac{\partial^2\psi}{\partial y\partial z} + N^2\frac{\partial^2\psi}{\partial y^2} = 0, \tag{37}$$

where $v' = \partial\psi/\partial z$ and $w' = -\partial\psi/\partial y$ are the instabilities' meridional and vertical velocities, respectively (Hoskins, 1974). If there are no boundaries, solutions of the form of plane waves $\psi = \Re\{\Psi \exp[\sigma t + i(ly+mz)]\}$ can be sought, where l,m are the components of the wavevector and σ is the growth rate. Substituting this ansatz into (37) yields an equation for the growth rate: $\sigma^2 = -N^2\sin^2\alpha - F^2\cos^2\alpha + M^2\sin 2\alpha$, where $\alpha = -\tan^{-1}(l/m)$ is the angle that the velocity vector in the y–z plane makes with the horizontal. Each mode, with angle α and vertical wavenumber m, has buoyancy and zonal velocity anomalies, $(b',u') = \Re\{(B,U)\exp[\sigma t + i(ly+mz)]\}$ with amplitudes

$$B = i\frac{m}{\sigma}(M^2 - N^2\tan\alpha)\Psi, \tag{38}$$

$$U = i\frac{m}{f\sigma}(F^2 - M^2\tan\alpha)\Psi. \tag{39}$$

The modes that maximize or minimize the growth rate are characterized by velocity vectors with angles

$$\alpha_{0,1} = \frac{1}{2}\tan^{-1}\left(\frac{2M^2}{N^2-F^2}\right) + \frac{\pi}{2}n, \quad n = 0,1, \tag{40}$$

where $\alpha_{max} = \max(\alpha_0,\alpha_1)$ corresponds to the angle of the fastest growing mode.

The information from this simple linear stability analysis can be used to estimate the relative strength of the energy sources (10)–(12) of the fastest growing overturning instabilities that develop when $fq < 0$. Namely,

$$\left.\frac{\mathrm{BFLUX}}{\mathrm{GSP}}\right|_{\alpha_{max}} \sim \left.-\frac{w'b'}{w'u'(M^2/f)}\right|_{\alpha_{max}} = -\frac{(M^2 - N^2\tan\alpha_{max})}{(F^2 - M^2\tan\alpha_{max})}\left(\frac{f^2}{M^2}\right), \tag{41}$$

$$\left.\frac{\mathrm{LSP}}{\mathrm{GSP}}\right|_{\alpha_{max}} \sim \left.\frac{u'v'(f^2-F^2)/f}{w'u'(M^2/f)}\right|_{\alpha_{max}} = \frac{(1-F^2/f^2)}{\tan\alpha_{max}}\left(\frac{f^2}{M^2}\right). \tag{42}$$

The dependence of these ratios on M^2 and N^2 is shown in Fig. 15 for a background flow with anticyclonic vorticity and absolute vorticity $F^2/f = 0.4f$. As can be seen in the figure, the ratios are highly dependent of the angle ϕ_{Ri_B}. The buoyancy flux exceeds the geostrophic shear production only for ϕ_{Ri_B} less than -135°. Thus below this angle the instability transitions to convection. For $-135^\circ < \phi_{Ri_B} - 90^\circ$ the instability gets its energy primarily from the vertical shear of the geostrophic flow and secondarily from the convective available potential energy. When the stratification is stable, i.e. $\phi_{Ri_B} > -90^\circ$, the buoyancy flux plays a minimal role in the energetics of the instabilities. This is because for these values of ϕ_{Ri_B} the fastest growing mode has flow that is nearly parallel to isopycnals and thus $B \approx 0$. For $-90^\circ < \phi_{Ri_B} - 45^\circ$ the instability gets its energy primarily from the vertical shear of the geostrophic flow and secondarily from its lateral shear. Above $\phi_{Ri_B} = -45^\circ$, and for sufficiently strong anticyclonic vorticity, LSP/GSP becomes larger than one, indicating a transition from symmetric to centrifugal/inertial instability. The boundaries marking the transitions between gravitational, symmetric, and inertial/centrifugal instability based on this linear stability analysis are schematized in Fig. 1.

References

Allen, J.T., Smeed, D.A., 1996. Potential vorticity and vertical velocity at the Iceland–Faeroes front. J. Phys. Oceanogr. 26, 2611–2634.

Belkin, I.M., Cornillon, P.C., Sherman, K., 2009. Fronts in large marine ecosystems. Prog. Oceanogr. 81, 223–236.

Bennetts, D.A., Hoskins, B.J., 1979. Conditional symmetric instability—a possible explanation for frontal rainbands. Q. J. R. Met. Soc. 105, 945–962.

Boccaletti, G., Ferrari, R., Fox-Kemper, B., 2007. Mixed layer instabilities and restratification. J. Phys. Oceanogr. 37, 2228–2250.

Capet, X., McWilliams, J.C., Molemaker, M.J., Shchepetkin, A.F., 2008. Mesoscale to submesoscale transition in the California Current system. Part III: energy balance and flux. J. Phys. Oceanogr. 38, 2256–2269.

D'Asaro, E., Lee, C.M., Rainville, L., Harcourt, R., Thomas, L.N., 2011. Enhanced turbulence and energy dissipation at ocean fronts. Science 332, 318–332, http://dx.doi.org/10.1126/science.1201515.

Ferrari, R., Wunsch, C., 2009. Ocean circulation kinetic energy: reservoirs, sources, and sinks. Annu. Rev. Fluid Mech. 41, 253–282.

Fox-Kemper, B., Ferrari, R., Hallberg, R., 2008. Parameterization of mixed layer eddies. Part I: theory and diagnosis. J. Phys. Oceanogr. 38, 1145–1165.

Gill, A.E., Green, J.S.A., Simmons, A.J., 1974. Energy partition in the large-scale ocean circulation and the production of mid-ocean eddies. Deep-Sea Res. 21, 499–528.

Haine, T.W.N., Marshall, J., 1998. Gravitational, symmetric, and baroclinic instability of the ocean mixed layer. J. Phys. Oceanogr. 28, 634–658.

Hoskins, B.J., 1974. The role of potential vorticity in symmetric stability and instability. Q. J. R. Met. Soc. 100, 480–482.

Hoskins, B.J., 1982. The mathematical theory of frontogenesis. Annu. Rev. Fluid Mech. 14, 131–151.

Hoskins, B.J., Draghici, I., Davies, H.C., 1978. A new look at the omega-equation. Q. J. R. Met. Soc. 104, 31–38.

Inoue, R., Gregg, M.C., Harcourt, R.R., 2010. Mixing rates across the Gulf Stream, Part 1: on the formation of Eighteen Degree Water. J. Mar. Res. 68, 643–671.

Joyce, T.M., Thomas, L.N., Bahr, F., 2009. Wintertime observations of Subtropical Mode Water formation within the Gulf Stream. Geophys. Res. Lett. 36, L02607, http://dx.doi.org/10.1029/2008GL035918.

Large, W.G., McWilliams, J.C., Doney, S.C., 1994. Oceanic vertical mixing: a review and a model with a nonlocal boundary layer parameterization. Rev. Geophys. 32, 363–403.

Le Traon, P.Y., 1990. A method for optimal analysis of fields with spatially variable mean. J. Geophys. Res. 95 (C8), 13543–13547.
Marshall, J., et al., 2009. The Climode field campaign: observing the cycle of convection and restratification over the Gulf Stream. Bull. Am. Meteor. Soc. 90, 1337–1350.
Marshall, J., Schott, F., 1999. Open ocean deep convection: observations, models and theory. Rev. Geophys. 37, 1–64.
Marshall, J.C., Nurser, A.J.G., 1992. Fluid dynamics of oceanic thermocline ventilation. J. Phys. Oceanogr. 22, 583–595.
Maze, G., Marshall, J., 2011. Diagnosing the observed seasonal cycle of Atlantic subtropical mode water using potential vorticity and its attendant theorems. J. Phys. Oceanogr. 41, 1986–1999.
McWilliams, J.C., Sullivan, P.P., Moeng, C.H., 1997. Langmuir turbulence in the ocean. J. Fluid Mech. 334, 1–30.
Molemaker, J., McWilliams, J.C., Capet, X., 2010. Balanced and unbalanced routes to dissipation in an equilibrated Eady flow. J. Fluid Mech. 654, 35–63.
Naveira Garabato, A., Polzin, K., King, B., Heywood, K., Visbeck, M., 2004. Widespread intense turbulent mixing in the Southern Ocean. Science 303, 210–213.
Naveira Garabato, A.C., Allen, J.T., Leach, H., Strass, V.H., Pollard, R.T., 2001. Mesoscale subduction at the Antarctic Polar Front driven by baroclinic instability. J. Phys. Oceanogr. 31, 2087–2107.
Nikurashin, M., Ferrari, R., 2010. Radiation and dissipation of internal waves generated by geostrophic motions impinging on small-scale topography: application to the Southern Ocean. J. Phys. Oceanogr. 40, 2025–2042.
Pollard, R.T., Regier, L.A., 1992. Vorticity and vertical circulation at an ocean front. J. Phys. Oceanogr. 22, 609–625.
Price, J.F., Weller, R.A., Pinkel, R., 1986. Diurnal cycling: observations and models of the upper ocean response to diurnal heating, cooling, and wind mixing. J. Geophys. Res. 91, 8411–8427.
Ruddick, B.R., 1983. A practical indicator of the stability of the water column to double-diffusive activity. Deep-Sea Res. 30, 1105–1107.
Rudnick, D.L., 1996. Intensive surveys of the Azores Front. 2. Inferring the geostrophic and vertical velocity fields. J. Geophys. Res. 101 (C7), 16291–16303.
Stone, P., 1970. On non-geostrophic baroclinic stability: Part II. J. Atmos. Sci. 27, 721–726.
Taylor, J., Ferrari, R., 2009. The role of secondary shear instabilities in the equilibration of symmetric instability. J. Fluid Mech. 622, 103–113.
Taylor, J., Ferrari, R., 2010. Buoyancy and wind-driven convection at mixed-layer density fronts. J. Phys. Oceanogr. 40, 1222–1242.
Taylor, J., Ferrari, R., 2011. Ocean fronts trigger high latitude phytoplankton blooms. Geophys. Res. Lett. 38, L23601.
Thomas, L.N., 2005. Destruction of potential vorticity by winds. J. Phys. Oceanogr. 35, 2457–2466.
Thomas, L.N., Joyce, T.M., 2010. Subduction on the northern and southern flanks of the Gulf Stream. J. Phys. Oceanogr. 40, 429–438.
Thomas, L.N., Lee, C.M., 2005. Intensification of ocean fronts by down-front winds. J. Phys. Oceanogr. 35, 1086–1102.
Thomas, L.N., Lee, C.M., Yoshikawa, Y., 2010. The Subpolar Front of the Japan/East Sea II: inverse method for determining the frontal vertical circulation. J. Phys. Oceanogr. 40, 3–25.
Thomas, L.N., Taylor, J.R., 2010. Reduction of the usable wind-work on the general circulation by forced symmetric instability. Geophys. Res. Lett. 37, L18606, http://dx.doi.org/10.1029/2010GL044680.
Thorpe, A.J., Rotunno, R., 1989. Nonlinear aspects of symmetric instability. J. Atmos. Sci. 46, 1285–1299.

Please cite this article as: Thomas, L.N., et al., Symmetric instability in the Gulf Stream. Deep-Sea Res. II (2013), http://dx.doi.org/10.1016/j.dsr2.2013.02.025